

Article

Modeling Analysis of Bi-Layer Ni-(ZrO₂)_x(Y₂O₃)_{1-x} Anodes for Anode-Supported Intermediate Temperature-Solid Oxide Fuel Cells

Anna Enrico, Marco Cannarozzo and Paola Costamagna *

Department of Civil, Chemical and Environmental Engineering (DICCA),
Polytechnic School, University of Genoa, Via Opera Pia 15, 16145 Genoa, Italy;
E-Mails: anna.enrico@edu.unige.it (A.E.); marco.cannarozzo@libero.it (M.C.)

* Author to whom correspondence should be addressed; E-Mail: paola.costamagna@unige.it;
Tel.: +39-010-353-2922; Fax: +39-010-353-2586.

Received: 26 June 2014; in revised form: 1 August 2014 / Accepted: 1 August 2014 /

Published: 28 August 2014

Abstract: Intermediate temperature-solid oxide fuel cell (IT-SOFC) Ni-(ZrO₂)_x(Y₂O₃)_{1-x} (Ni-YSZ) anodes formed by two layers, with different thicknesses and morphologies, offer the possibility of obtaining adequate electrochemical performance coupled to satisfactory mechanical properties. We investigate bi-layered Ni-YSZ anodes from a modeling point of view. The model includes reaction kinetics (Butler-Volmer equation), mass transport (Dusty-Gas model), and charge transport (Ohm's law), and allows to gain an insight into the distribution of the electrochemical reaction within the electrode. Additionally, the model allows to evaluate a reciprocal overall electrode resistance $1/R_p \approx 6 \text{ S}\cdot\text{cm}^{-2}$ for a bi-layer electrode formed by a 10 μm thick active layer (AL) composed of 0.25 μm radius Ni and YSZ particles (34% vol. Ni), coupled to a 700 μm thick support layer (SL) formed by 0.5 μm radius Ni and YSZ particles (50% vol. Ni), and operated at a temperature of 1023 K. Simulation results compare satisfactorily to literature experimental data. The model allows to investigate, in detail, the effect of morphological and geometric parameters on the various sources of losses, which is the first step for an optimized electrode design.

Keywords: intermediate temperature-solid oxide fuel cell (IT-SOFC); Ni-(ZrO₂)_x(Y₂O₃)_{1-x} (Ni-YSZ) composite; anode; anode-supported cell; bi-layer electrode; modeling

1. Introduction

Solid oxide fuel cells (SOFCs) offer an electrochemical energy conversion technology featuring high efficiency and low pollution emissions. Their reliability, modularity, and fuel adaptability make them good candidates for substituting, at least in some applications, more conventional energy conversion systems [1–6]. SOFCs, traditionally, operate at high temperatures (1050–1300 K), but the research trend in recent years is to reduce the operating temperature to a range of 750–1100 K [7], with the development of intermediate temperature-SOFCs (IT-SOFCs). In fact, a lower operating temperature would mitigate various problems, such as gas leakage, formation of an insulating layer at the electrode/electrolyte (E/E) interface, and crack formation from stresses caused by large differences in thermal expansion coefficients (TEC) of the cell components [4]. Additional benefits include a wider choice of materials and a significantly improved stability and reliability of the components of the SOFC system.

Lowering the operating temperature also lowers the fuel cell performance, since the kinetics of the electrochemical reaction decreases rapidly as temperature decreases. Furthermore, the electrodes and electrolyte materials become less conductive [8], leading to higher ohmic losses. Considering the overall cell performance, the ohmic losses are dominated primarily by the electrolyte contribution [9]. Among the electrolyte materials, $(\text{ZrO}_2)_x(\text{Y}_2\text{O}_3)_{1-x}$ (YSZ) is still one of the most widely used for its stability in both reducing and oxidizing conditions, even if its oxygen-ion conductivity is lower than that of other ceramics, such as doped ceria and $\text{La}_x\text{Sr}_{1-x}\text{Ga}_y\text{Mg}_{1-y}$ (LSGM) [10]. This has led to the necessity of developing a very thin electrolyte (5–15 μm) in order to minimize performance losses [11,12]. Thus, it is evident that an electrode-supported SOFC design is more suitable for operation at low temperatures than an electrolyte-supported one. Since in the operating temperature range of IT-SOFCs, cathode voltage losses are up to one order of magnitude higher than the corresponding anodic losses [8], the anode is the best choice to perform as a support. For this reason, among the various IT-SOFC geometries proposed in the literature, the anode-supported type has been extensively studied [1,13]. In this design, the anode has to ensure both electrochemical and mechanical requirements, often conflicting with each other. For example, from a mechanical point of view, in the anode-supported design, the anode is responsible for the structural integrity and reliability of the cell, and a high thickness is necessary to ensure an adequate mechanical resistance. Additionally, the electrode porosity needs an accurate tuning, since a high porosity affects severely the hardness of the anode [14]. On the other hand, from the electrochemical point of view, the anode performance is affected by different types of losses, namely, (i) ohmic polarization, related to the ionic and electronic conducting paths into the electrode; it is reduced by short conduction paths and high conductivities; (ii) activation polarization, which is the voltage loss associated with the hydrogen electro-oxidation reaction; it is reduced if a wide three phase boundary (TPB) area is available to the electrochemical reaction [15]; (iii) concentration polarization, due to sluggish transport of gaseous species through the electrode; it is reduced in case of large pores and short diffusion paths [16]. Thus, in contrast with the needs related to the mechanical requirements, the electrochemical requirements lead to thin and highly porous anodes. In order to conciliate mechanical and electrochemical needs, multi-layer electrodes have been proposed, consisting of two (or even more) different homogeneous layers. The anode is, thus, divided into a thick (between 0.5 mm and 1.5 mm) highly porous support layer (SL), enabling fast gas and electron transport, and, close to the electrolyte,

a thin (5–20 μm) active layer (AL) devoted to the electrochemical reaction, with a finer microstructure in order to increase the TPB [17–19].

Recently, a wide range of materials for SOFC anodes has been proposed and investigated, especially in view of enlarging the choice of fuel compositions [19]. Among them, traditional Ni-YSZ cermets developed for high temperature-SOFC (HT-SOFC) are widely employed, even for IT-SOFC applications, because of the low cost and TEC values close to that of the dense YSZ electrolyte, which prevents cracking and consequent gas leakages caused by thermal cycling [20]. The Ni-YSZ cermet structure also displays satisfactory adhesion to the YSZ electrolyte [19,21], and achieves large electrochemical active area by extending the TPB from the anode/electrolyte interface into the porous anode. The necessity of an accurate tailoring of the electrode composition has been demonstrated for single layer electrodes, and is even more important if there are different layers coexisting in the same anode structure [22,23]. Thus, regarding the composition of bi-layered Ni-YSZ electrodes, usually the SL contains a high amount of electronic conductor, in order to have a good electrical contact with the interconnector and to act as a current collector for the AL. Instead, the AL contains a prevailing amount of ionic conductor, in order to enhance the conduction of the oxygen ions coming from the electrolyte, and also to enhance adhesion to the electrolyte. The different composition of the AL and SL is an important factor, also in view of providing a gradual variation of TEC across the anode, in order to prevent possible delamination [24]. An overview of the AL and SL features is given in Table 1.

Table 1. Typical features of bi-layer anodes [9–11,17–19,22–24]. SL: support layer; and AL: active layer.

Feature	SL	AL
Function	mechanical support; electron transport; and gas diffusion	electrochemical reaction
Thickness	up to 2 mm	5–20 μm
Percolation	ionic	not strictly necessary
	electronic	yes
Particle radius	0.25 $\mu\text{m} < r < 1.5 \mu\text{m}$	0.05 $\mu\text{m} < r < 0.5 \mu\text{m}$
Pore radius	0.25 $\mu\text{m} < r < 1.5 \mu\text{m}$	0.05 $\mu\text{m} < r < 0.5 \mu\text{m}$
Porosity	40%–50%	20%–30%

To the best of the authors' knowledge, bi-layered IT-SOFC anodes have not yet been investigated from a theoretical point of view. Instead, some modelling studies have been devoted to functionally graded electrodes (FGEs) for SOFC applications. Greene *et al.* [25] have developed a numerical model to investigate mass transport in porosity-graded electrodes. They have considered the electrochemical reaction to occur merely at the E/E interface, and they have highlighted that, increasing the electrode porosity towards the E/E interface, better performance is achieved. Ni *et al.* [26,27] have investigated the effect of particle size grading on the performance of SOFC anodes and complete cells employing FGEs. The authors have taken into account composite anodes formed by a mixture of electronic and ionic conducting particles. They have considered the electrochemical reaction to extend within the electrode thickness, and they have pointed out that particle size grading allows to obtain better performance than porosity grading, due to reduced mass transport resistance and increased TPB close

to the E/E interface. They have underlined that this effect is more evident in thick electrodes, considering a maximum electrode thickness of about 500 μm [27]. Other works have focused on the optimization of morphological parameters of SOFC FGEs. Lee *et al.* [28] have analysed the influence of different particle size grading profiles on complete SOFC performance. Shi *et al.* [29] have developed a genetic algorithm to optimize porosity and particle size distribution, confirming that FGEs show better performance than homogeneous electrodes, but also showing that the optimized design depends on the operating conditions. Other authors have studied the effects of grading composition and morphological parameters in cathodes: Deseur *et al.* [30,31] have investigated how graded composition can increase cathode performance, demonstrating that the improvements can be further enhanced if associated with particle size grading.

In this framework, our work deals with the simulation of bi-layered anodes for anode-supported IT-SOFCs: unlike the literature models previously discussed, we consider the anode as composed by two different physical layers, AL and SL, which have porosity, particle size and composition internally homogeneous, but different from each other. The electrode properties do not vary gradually along the electrode thickness (as in FGEs), but they vary sharply from the AL to the SL. Furthermore, our anodes are thick (up to 2 mm), since they must provide mechanical support to the fuel cell, while the FGEs investigated in the literature usually do not have this support function and are significantly thinner (maximum thickness about 500 μm [27]). The specific problem of designing the SL so that the presence of this thick layer does not hinder the electrochemical performance of the overall electrode is addressed here.

Our theoretical investigation is based on a validated electrochemical model developed for a random-packing Ni-YSZ single-layer HT-SOFC anode [16,32–34], updated for application to IT-SOFCs. The model is thus applied in the same form to both the AL and SL layers. In this sense, our approach is different from that pursued in previous literature [35], where the possibility of simulating a homogeneous one-layer anode as a fictitious bi-layer anode has been investigated. This latter method has involved a first step of identification of the electrochemically active thickness (EAT) [36], defined as the electrode thickness close to the E/E interface where 99% of the electrochemical reaction takes place (*i.e.*, 99% of the ionic current is transferred into electronic current). Then, the possibility of simulating the EAT through a detailed approach, and the remaining part of the electrode through a simplified approach, has been demonstrated, with interesting computational advantages [35]. In [35], the EAT has been proved to grow by increasing the operating temperature. The extension of the EAT has been further investigated in a recent literature work [36], where it has been demonstrated to increase by decreasing the exchange current density of the electrochemical reaction or the effective ionic resistivity of the electrode.

In the present work, we adopt a slightly different definition of EAT, *i.e.*, the electrode thickness close to the E/E interface where 95% of the electrochemical reaction takes place. In addition, we wish to underline that, in the present work, AL and EAT do not coincide. The thickness of the AL is the physical thickness of the electrode layer adjacent to the electrolyte. On the other hand, the thickness of the EAT is investigated on the basis of the model, and it is shown to be completely included into the AL in some cases, and to extend beyond the AL, with penetration into the SL, in other cases.

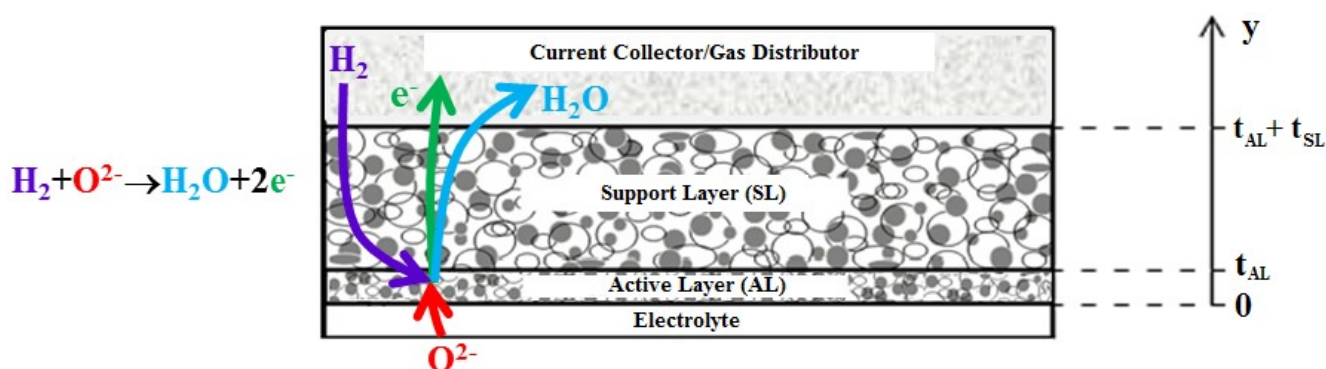
The aim of the present paper is to investigate bi-layered anodes for anode-supported IT-SOFCs, and in particular to study how the microstructure, geometry and composition of each layer influence

the overall anode electrochemical performance, by analysing the effect of the various parameters on each individual source of loss occurring in the AL and in the SL. Simulation results are compared to literature experimental data demonstrating good agreement. The ultimate goal is to contribute to the design of bi-layered anodes for anode-supported IT-SOFCs, which retain the beneficial properties of both the AL and SL layers, reducing the related drawbacks.

2. Model

The model is developed with reference to the bi-layer anode schematized in Figure 1. As mentioned above, the bi-layer anode is composed by a thick SL adjacent to the current collector, enabling fast gas and electron transport, and a thin AL adjacent to the electrolyte, with a finer microstructure in order to increase the TPB and enhance the electrochemical reaction.

Figure 1. Scheme of a Ni-(ZrO₂)_x(Y₂O₃)_{1-x} (Ni-YSZ) bi-layer anode.



The main hypotheses of the model are summarized below:

- steady-state conditions;
- uniform temperature and pressure throughout the electrode;
- one-dimensional model as a function of the y coordinate (Figure 1);
- each layer is a random packing of Ni and YSZ particles;
- in each layer, the particles of the same type (Ni or YSZ) are supposed to be all spherical and of identical size.

Only the main equations of the model are recalled here; a complete description can be found in [16]. The model is composed by two parts: an electrochemical one (Equations (1)–(3)), including charge transport, charge balance and local electrochemical kinetics, and a mass diffusion part (Equations (5)–(9)), taking into account local mass balances and mass transport equations.

In the electrochemical part of the model (Equation (1)), Ohm's law is applied for the charge transport of both the ionic and electronic species, and i_{io} and i_{el} are the ionic and electronic current densities, which are considered as positive and are referred to the electrode surface. i_n expresses the electrochemical reaction rate, resulting in a transfer of charge from i_{io} to i_{el} ; i_n is a current density referred to the extension of the active area available for the electrochemical reaction (A , active area per unit volume of the electrode):

$$\left\{ \begin{array}{l} \frac{dV_{io}}{dy} = \rho_{io}^{eff} i_{io} \\ \frac{dV_{el}}{dy} = \rho_{el}^{eff} i_{el} \\ \frac{di_{el}}{dy} = A \cdot i_0 \left\{ \frac{p_{H_2}}{p_{H_2}^0} \exp\left(\frac{\beta \eta F}{RT}\right) - \frac{p_{H_2O}}{p_{H_2O}^0} \exp\left(-\frac{(1-\beta) \eta F}{RT}\right) \right\} = A \cdot i_n \\ \frac{di_{io}}{dy} = -\frac{di_{el}}{dy} \\ \eta = (V_{io}^{eq} - V_{el}^{eq}) - (V_{io} - V_{el}) \end{array} \right. \quad (1)$$

In Equation (1), i_n is evaluated through the current-overpotential equation, where i_0 is expressed as follows [37]:

$$i_0 = \gamma \left(\frac{p_{H_2}}{p_{ref}} \right) \left(\frac{p_{H_2O}}{p_{ref}} \right)^{-0.5} \exp\left(-\frac{E_{act}}{RT}\right) \quad (2)$$

Finally, in Equation (1), the charge conservation is expressed by the charge balance equation, and the definition of overpotential η is recalled.

Equation (1) contains a number of parameters, which are calculated through the percolation theory [38,39]. Percolation occurs when particles of the same type (ionic or electronic conductor) form an interconnected network through the electrode, spanning throughout the whole electrode thickness. If the ratio between electrode thickness and electrode particle diameter is larger than about 20–40, then percolation occurs sharply for a well-defined electrode composition termed percolation threshold [33]. The electrode has two percolation thresholds, ionic and electronic. In the present work, the percolation thresholds and also some model parameters appearing in Equation (1), such as the effective resistivities ρ^{eff} and the active area for the electrochemical reaction A , are evaluated through the percolation theory, following the approach presented in [33].

Concerning the effective resistivity ρ^{eff} , if the content of one type of conducting particles is below the percolation threshold, the corresponding ρ^{eff} tends to infinity, while for compositions above the percolation threshold, the resistivity is quickly reduced, towards the resistivity of the bulk material [33]. This holds for both the electronic conductor (Ni) and the oxygen-ion conductor (YSZ). In our model, the bulk electronic resistivity of Ni is approximated as constant with temperature (Table 2), while the bulk ionic resistivity of YSZ is assumed as temperature dependent [40]:

$$\rho_{io} = \rho_{io}^0 \exp\left(\frac{E'_{act}}{RT}\right) \quad (3)$$

Concerning the active area for the electrochemical reaction A , this is strictly related to the TPB, and it is zero at and outside the percolation thresholds. Inside the percolation thresholds, A tends to zero when approaching the percolation thresholds, and it is maximum for intermediate compositions. Further, the smaller the electrode particles, the larger the active area A [33].

In the present work, Ni-YSZ layer compositions are expressed through ϕ , which is the volumetric fraction of particles of the same type (referring to the total solid volume, voids excluded) [33]. ϕ_{el} is the volumetric fraction of the electronic conducting particles (Ni), and ϕ_{io} (where $\phi_{io} = 1 - \phi_{el}$) is the volumetric fraction of the ionic conducting particles (YSZ). In particular, below, we will use ϕ_{el} to identify electrode layer composition. Coherently, the electrode composition at the percolation thresholds will be identified again through ϕ_{el} , for both the electronic and the ionic percolation thresholds.

Table 2. Base-case bi-layered Ni-YSZ anode: model parameters and operating conditions.

Parameter	SL	AL	Description
ρ_{io}^0, E'_{act}	$27.8 \times 10^3 \text{ S/m}, 9.8 \times 10^3 \text{ K}^{-1}$		Coefficients for evaluation of the YSZ bulk ionic resistivity, Equation (3) [40]
ρ_{el}	$5 \times 10^{-9} \text{ } \Omega \cdot \text{cm}$		Bulk Ni electronic resistivity [33]
γ, E_{act}	$5.5 \cdot 10^8 \text{ A/m}^2, 100 \times 10^3 \text{ J/mol}$		Exchange current density coefficients in Equation (2) [41]
β	0.5		Charge transfer coefficient, Equation (1) [42,43]
r_{el}	0.5 μm	0.25 μm	Electronic conductor radius
P	1		r_{io}/r_{el}
ϕ_{el}	0.5	0.44	Electronic conductor volumetric fraction
ε	0.5	0.2	Electrode porosity [44,45]
τ	2	2	Electrode tortuosity [44,46]
t	700 μm	10 μm	Layer thickness
$p_{H_2}^0, p_{H_2O}^0$	0.6 atm, 0.4 atm		H_2 and H_2O partial pressure in the feeding fuel ($y = t_{AL} + t_{SL}$)
I_{tot}	0.5 A/cm^2		Overall electrode current density
T	1073 K		Temperature

In the second part of the model, devoted to the analysis of mass transport and including local mass balances, we consider the semi-reaction occurring at the anodic side of an SOFC:



In an SOFC anode, the conversion of the oxygen ions and the formation of electrons are related to the consumption of H_2 and the formation of H_2O through the Faraday's law; in the light of this, the local mass balances can be written as follows:

$$\begin{cases} \frac{dN_{H_2}}{dy} = \frac{i_n}{2F} A \\ \frac{dN_{H_2O}}{dy} = -\frac{i_n}{2F} A \end{cases} \quad (5)$$

where N are molar fluxes; and F is the Faraday's constant. The Dusty Gas Model for diffusion in porous media [16,47,48], allows to derive the expressions of molar fluxes:

$$\begin{cases} N_{H_2} = \left(x_{H_2O} \left(\frac{1}{D_{H_2-H_2O}^{eff}} + \frac{1}{D_{H_2,K}^{eff}} \right)^{-1} + x_{H_2} \left(\frac{1}{D_{H_2-H_2O}^{eff}} + \frac{1}{D_{H_2,O,K}^{eff}} \right)^{-1} \right) \cdot \frac{1}{RT} \frac{dp_{H_2}}{dy} \\ N_{H_2O} = \left(x_{H_2O} \left(\frac{1}{D_{H_2-H_2O}^{eff}} + \frac{1}{D_{H_2,K}^{eff}} \right)^{-1} + x_{H_2} \left(\frac{1}{D_{H_2-H_2O}^{eff}} + \frac{1}{D_{H_2,O,K}^{eff}} \right)^{-1} \right) \cdot \frac{1}{RT} \frac{dp_{H_2O}}{dy} \end{cases} \quad (6)$$

The term $\left(x_{H_2O} \left(\frac{1}{D_{H_2-H_2O}^{eff}} + \frac{1}{D_{H_2,K}^{eff}} \right)^{-1} + x_{H_2} \left(\frac{1}{D_{H_2-H_2O}^{eff}} + \frac{1}{D_{H_2,O,K}^{eff}} \right)^{-1} \right)$ is the effective diffusivity of the

gaseous mixture, and it is a function of composition and of both molecular and Knudsen diffusivities. The Knudsen diffusivities D_K^{eff} play a role when diffusion occurs in a porous medium with pore diameter smaller than the mean free path of the diffusing molecules. At 1073 K, the mean free path is about 3 μm for H₂, and about 0.9 μm for H₂O. In solids formed by a random packing of bimodal spheres, the average pore radius is related to the radius of the electrode particles through the following equation [47,48]:

$$r_{pore} = \frac{1}{1 - \epsilon} \cdot \left(\frac{\phi_{el}}{r_{el}} + \frac{1 - \phi_{el}}{r_{io}} \right)^{-1} \quad (7)$$

where ϕ_{el} is the volumetric fraction of the electronic conducting particles; and r_{el} and r_{io} are the radii of the electronic and ionic conducting particles respectively. Knudsen diffusivities are expressed according to the equation below [49]:

$$D_{i,K}^{eff} = \frac{\epsilon}{\tau} \cdot 97 \cdot r_{pore} \sqrt{\frac{T}{M_i}} \quad (8)$$

Molecular diffusivities are expressed by [49]:

$$D_{H_2-H_2O}^{eff} = \frac{\epsilon}{\tau} \cdot 0.0018583 \left(\frac{1}{M_{H_2}} + \frac{1}{M_{H_2O}} \right)^{1/2} \frac{T^{3/2}}{p \cdot \sigma^2 \cdot \Omega} \quad (9)$$

The two parts of the model, electrochemical and mass diffusion, are solved contemporarily, since electrical currents and mass fluxes are linked to each other at each point in the electrode. The model, as described above, is applied to both layers of the anode (AL: $0 < y < t_{AL}$; SL: $t_{AL} < y < t_{AL} + t_{SL}$). The chemical-physical features, *i.e.*, the active area (A), the effective diffusivities ($D_{H_2}^{eff}$ and $D_{H_2O}^{eff}$) and the effective resistivities (ρ_{el}^{eff} and ρ_{io}^{eff}), are calculated on the basis of the characteristics of each single layer. The following boundary conditions apply:

$$\begin{cases} y = 0 & i_{io} = I_{TOT} & i_{el} = 0 & \frac{dp_{H_2}}{dy} = 0 & \frac{dp_{H_2O}}{dy} = 0 \\ y = t_{AL} + t_{SL} & i_{io} = 0 & i_{el} = I_{TOT} & p_{H_2} = p_{H_2}^0 & p_{H_2O} = p_{H_2O}^0 \end{cases} \quad (10)$$

The boundary conditions state that the current is totally ionic at the E/E boundary, while it is totally electronic at the electrode/current-collector (E/CC) boundary; in both cases it is equal to the overall

electrode current I_{tot} . Additionally, since the electrolyte is gas-proof, the gaseous fluxes are zero at the E/E boundary, while the composition of the inlet fuel is known ($p_{\text{H}_2}^0, p_{\text{H}_2\text{O}}^0$) at the E/CC boundary.

At the interface between the two layers ($y = t_{\text{AL}}$) the following additional boundary conditions apply, which express the continuity of all the fluxes (electrons, ions, hydrogen, and water):

$$\begin{cases} i_{\text{io}}|_{t_{\text{AL}}^-} = i_{\text{io}}|_{t_{\text{AL}}^+} \\ i_{\text{el}}|_{t_{\text{AL}}^-} = i_{\text{el}}|_{t_{\text{AL}}^+} \\ N_{\text{H}_2}|_{t_{\text{AL}}^-} = N_{\text{H}_2}|_{t_{\text{AL}}^+} \\ N_{\text{H}_2\text{O}}|_{t_{\text{AL}}^-} = N_{\text{H}_2\text{O}}|_{t_{\text{AL}}^+} \end{cases} \quad (11)$$

From a mathematical point of view, this is a boundary value problem and it is solved numerically through Matlab[®]. Simulations are run in galvanostatic mode, *i.e.*, the overall electrode current density I_{tot} is an input of the model. Upon mathematical solution of the system of equations, the overall electrode overpotential η_{tot} is evaluated [33]:

$$\eta_{\text{tot}} = (V_{\text{io}}^{\text{eq}} - V_{\text{el}}^{\text{eq}}) - (V_{\text{io}}|_{y=0} - V_{\text{el}}|_{y=t_{\text{AL}}+t_{\text{SL}}}) \quad (12)$$

This quantity takes into account all types of losses, namely activation, ohmic and concentration losses. The performance of the anode is then evaluated in terms of an overall reciprocal resistance $1/R_p$, defined as follows:

$$\frac{1}{R_p} = \left(\frac{I_{\text{tot}}}{\eta_{\text{tot}}} \right) \quad (13)$$

3. Results

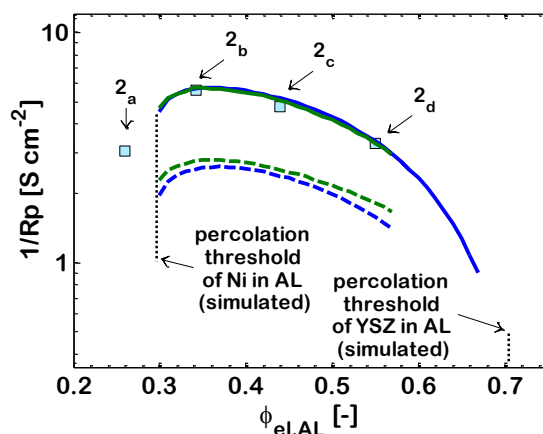
Results are reported with reference to a base-case bi-layer Ni-YSZ anode, whose features are summarized in Table 2. Both porosity and tortuosity, which characterize the diffusion of species in porous media, are from literature data [44,45]. A high gas-phase tortuosity of the anode can inhibit the transport of gaseous reactants and products, limiting the cell performance, especially at high fuel utilization. Wilson *et al.* [44] utilized three-dimensional reconstruction of a Ni-YSZ anode, based on finite element simulation, measuring a tortuosity factor between 1.9 and 2.2. Tortuosity values in the same range (1.77–2.16) are reported by [46]. In agreement with these data, we assume a tortuosity factor of two, as reported in Table 2.

In the present work, the electrode performance is calculated as an overall reciprocal electrode resistance $1/R_p$, defined through Equation (13). $1/R_p$ includes all types of losses and is calculated at a current density of 0.5 A/cm^2 . Results are presented together with a parametric analysis, which investigates the effect of the various morphological and geometrical parameters on $1/R_p$. In particular, the effect of the AL features is investigated in Sections 3.3–3.5, while Section 3.6 is devoted to the SL.

3.1. Model Validation

At first, we compare our model results to literature experimental data. The comparison is reported in Figure 2, where the experimental data are from [50], and refer to a bi-layer anode with a 10- μm thick AL and a 700- μm thick SL (in line with the data in Table 2). The literature experimental data have been obtained for four different Ni-YSZ compositions of the AL, labeled in Figure 2 as 2_a, 2_b, 2_c, and 2_d, corresponding to values of $\phi_{\text{el,AL}} = 0.26, 0.34, 0.44,$ and 0.55 , respectively. Porosities are reported in Table 2, as well as all the material properties and morphological parameters of the electrode. The literature experimental data have been obtained at 1073 K through the electrochemical impedance spectroscopy (EIS) technique. Figure 2 reports simulation results for several operating temperatures and current densities, and also for several volume fractions of Ni in the AL. The effect of each of these parameters on the electrode performance will be discussed in detail in the subsequent sections; here, we discuss only the good agreement between literature experimental data and simulation results obtained at 1073 K. The average error is about 2%; when calculating the error, the point labeled as 2_a is not taken into account because, as further discussed in the subsequent Section 3.3, it cannot be simulated through our model.

Figure 2. $1/R_p$ of bi-layered Ni-YSZ anodes operating at: $T = 973$ K (dashed lines); and $T = 1073$ K (solid lines); overall current density: — $I_{\text{tot}} = 1$ A/cm²; and — $I_{\text{tot}} = 0.5$ A/cm². Lines: simulation. Points: literature experimental data (2_a, 2_b, 2_c and 2_d) [50].



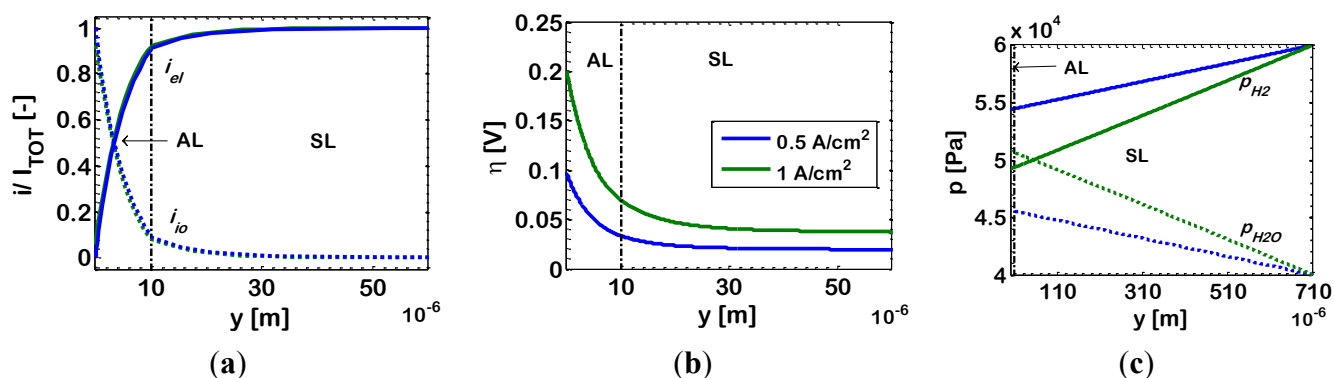
3.2. Effect of Operating Parameters: Current Density and Temperature

HT-SOFCs typically display a linear V - I curve, which is explained considering that the $1/R_p$ of their electrodes is independent of the applied current. This is due to the fact that diffusive losses (non-linear) are often negligible, and activation losses are linear due to the high operating temperature [43]. Instead, in IT-SOFC electrodes, due to the reduced operating temperature, depending on the electrode characteristics, diffusive losses can play a major role, and also activation losses can be non-linear [51], and actually both linear and non-linear IT-SOFC V - I curves are reported experimentally. In the case of the bi-layered IT-SOFC anodes under consideration, the effect of the current density is investigated in Figure 2, which reports $1/R_p$ simulation results for different applied currents and different operating temperatures. Figure 2 displays that, for the bi-layer electrode under analysis here, the simulation

results indicate that the electrode $1/R_p$ is practically identical for both the simulated operating currents (1 A/cm^2 and 0.5 A/cm^2), at each simulated operating temperature (973 K and 1073 K). Other simulations run for different current densities and not reported here confirm this result. This is validated by further literature experimental data collected from complete IT-SOFC cells employing anodes similar to those simulated in Figure 2 [50]. These literature results report $V-I$ characteristic curves which clearly display that the anodic loss is a main source of cell loss, and at the same time show linear behavior up to 2 A/cm^2 and further.

In order to explain this result, in Figure 3 we report simulations for the distributions of dimensionless current density i/I_{tot} , overpotential η , and partial pressures of hydrogen (p_{H_2}) and water ($p_{\text{H}_2\text{O}}$), along the anode thickness. Simulations are performed for an AL composition 2_c ($\phi_{\text{el,AL}} = 0.44$), temperature of 1073 K and for the operating currents already investigated in Figure 2, namely 1 A/cm^2 and 0.5 A/cm^2 . The simulated distributions of i/I_{tot} , η and P are discussed further in subsequent sections of this paper (in particular, Section 3.3.); here, we point the attention on the effects that the applied current has on the different sources of loss. Indeed, increasing the operating current density, two main effects occur at the same time, both related to the higher electrochemical reaction rate, *i.e.*, (i) a decrease of p_{H_2} , coupled to an increase of $p_{\text{H}_2\text{O}}$ (Figure 3c); and (ii) higher values of the overpotential η along the electrode (Figure 3b). The previous, is a diffusion-limitation effect, which normally leads to an increase of $1/R_p$ by increasing the current density (downward concavity of the $V-I$ curve). The latter, is an activation effect, which normally leads to a decrease of $1/R_p$ by increasing the current density (upward concavity of the $V-I$ curve). Here, these two effects compensate each other and the resulting i/I_{tot} profile along the electrode thickness is practically identical in both cases, as displayed in Figure 3a, and, thus, also the electrode $1/R_p$ is practically identical for both currents, as displayed in Figure 2.

Figure 3. Bi-layered Ni-YSZ anode with Ni volumetric fraction in the AL $\phi_{\text{el,AL}} = 0.44$ (Case 2_c). Simulation results at temperature $T = 1073 \text{ K}$; overall current density: — $I_{\text{tot}} = 1 \text{ A/cm}^2$, and — $I_{\text{tot}} = 0.5 \text{ A/cm}^2$: (a) ionic (dotted lines) and electronic (solid lines) currents densities; (b) overpotential (η); and (c) partial pressures of hydrogen (p_{H_2}) and water ($p_{\text{H}_2\text{O}}$).



For the anode under analysis, a compensation between activation and diffusive effects leads to linear behavior; however, for sake of completeness, we remark that also different behaviors are reported in the literature for experimental bi-layered IT-SOFC anodes with characteristics different from those reported in Table 2. Depending on the morphology and thickness of the various layers,

V - I curves, collected from complete IT-SOFCs in case where the anode is a main source of loss, can display a visible departure from linearity, with upward concavity (typical of activation effects and more visible at low operating current densities) [18,52], or downward concavity (typical of diffusion limitation effects and more visible at high operating current densities) [9]. In some cases, the V - I characteristic curves are very similar to those of low-temperature fuel cells, with a low-current density region with upward concavity related to activation losses, a linear intermediate region dominated by ohmic losses, and a high-current density region with downward concavity related to diffusive losses [53,54]. In other cases [9], experiments run with various electrodes with increasing porosity of the anode SL show that the concavity of the V - I curves changes from downward to upward, confirming the relationship between microstructure, relative importance of diffusion and activation losses, and shape of the V - I characteristic curves.

3.3. Effect of Ni-(ZrO₂)_x(Y₂O₃)_{1-x} Ratio in Active Layer

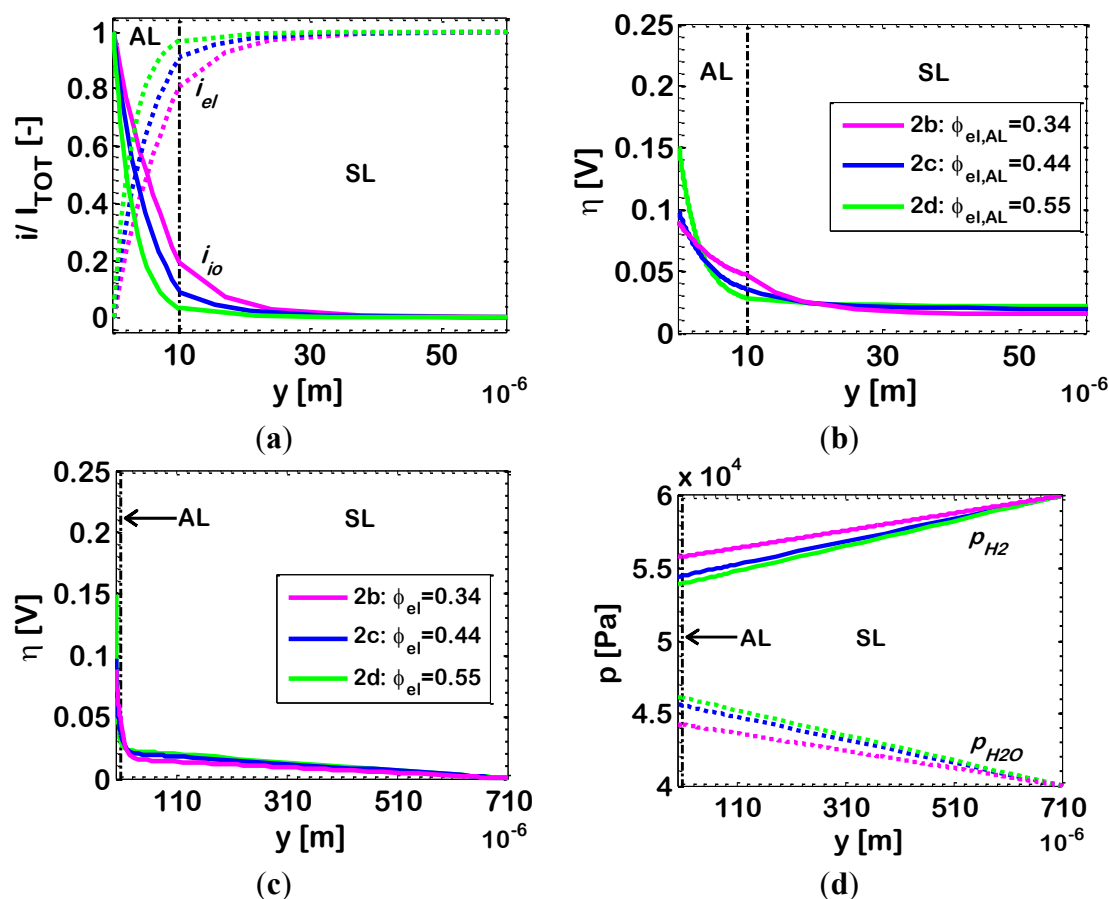
Figure 3 shows that, in bi-layered anodes, the electrochemical reaction takes place mainly in the AL. This is visible in particular from Figure 3a, which shows that the ionic current i_{io} entering the AL at the AL/electrolyte interface ($y = 0$), is quickly converted into electronic current i_{el} , due to the electrochemical reaction (Equation (4)). At the AL/SL interface ($y = 10 \mu\text{m}$), the ionic current is practically zero, and the electrochemical reaction is almost complete; the EAT is about $16 \mu\text{m}$, slightly larger than the AL. Since the electrochemical reaction occurs almost completely in the AL, the effect of the morphological and geometrical parameters of the AL on the overall electrode $1/R_p$ is somehow analogous to that reported previously for single-layer electrodes [16,33]. In particular, the composition of the AL in terms of Ni-YSZ content needs careful design, in order to remain in the window of compositions where both the ionic and the electronic conductors percolate, and this is clearly displayed in Figure 2, which reports the effect of varying ϕ_{el} in the AL, and also exhibits the simulated percolation thresholds of Ni and YSZ in the AL. From a theoretical point of view, in the case where the Ni and YSZ particles have the same dimensions, the percolation theory predicts percolation of the electronic conducting particles to occur for $\phi_{el} = 0.294$. Our model cannot simulate an electrode with Ni volumetric fraction lower than this value, because, in this situation, our model predicts that there are no clusters of electronic conducting particles spanning through the whole AL thickness. On the contrary, the literature experimental data reported in Figure 2 show that the real electrode with AL Ni content $\phi_{el,AL} = 0.26$ (slightly below the percolation threshold), tested in the experimental campaign, shows satisfactory performance. This indicates an imprecision in the evaluation of the theoretical percolation thresholds through the correlations of the classical percolation theory applied to SOFC electrodes, which has already been discussed in previous papers [33]. This imprecision can be due to a number of reasons, *i.e.*, (i) the correlations for the evaluation of percolation thresholds hold for a random packing of spheres with bimodal size: in reality, in the experimental electrodes, the particles are not perfectly spherical. Further, there is a particle size distribution for both the ionic and the electronic conductor, and also the average particle size is known with a certain measurement error; and (ii) in the experimental electrodes, when the ratio between the layer thickness and the particle size is below 20 (in the case under analysis, it is about 20) some short clusters of particles, which would not lead to percolation in thick electrodes, can nevertheless span throughout the whole layer. As a consequence,

the variation of properties across the percolation threshold is smooth, instead of being sharp. The consequences of this imprecision in the evaluation of percolation thresholds are expected to be significant only in a narrow range of compositions around the percolation thresholds themselves.

As displayed in Figure 2, the percolation theory predicts the percolation threshold of YSZ to occur for $\phi_{el} = 0.706$ (*i.e.*, $\phi_{io} = 0.294$), but, unluckily, no experimental data are available to confirm this result. Instead, other simulation results reported in Figure 2 are confirmed by the available experimental data, and show that the $1/R_p$ values obtained for compositions intermediate between the two percolation thresholds are very satisfactory for IT-SOFC applications. The behavior of $1/R_p$ versus $\phi_{el,AL}$ is qualitatively similar to that reported previously for Pt-YSZ single-layer HT-SOFC electrodes [55]. In particular, Figure 2 shows that a maximum is obtained around Point 2_b ($\phi_{el,AL} = 0.34$) for a Ni content in the AL about 10% higher than the theoretical percolation threshold; a similar finding was previously obtained also for single-layer HT-SOFC electrodes [55].

In Figure 4, we investigate this in further detail by analyzing the simulated distributions of dimensionless current density i/I_{tot} , overpotential η and partial pressures of hydrogen (p_{H_2}) and water (p_{H_2O}) along the electrode thickness. We simulate three different AL compositions corresponding to the Points 2_b, 2_c, and 2_d highlighted in Figure 2. For these simulations, we assume a current density of 0.5 A/cm^2 .

Figure 4. Bi-layered Ni-YSZ anodes at temperature $T = 1073 \text{ K}$ (other data in Table 2). Varying parameter: Ni volumetric fraction in the AL ($\phi_{el,AL}$). Simulated distributions along the electrode thickness of: (a) ionic (i_{io}) and electronic (i_{el}) currents; (b,c) overpotential (η); and (d) partial pressures of hydrogen (p_{H_2}) and water (p_{H_2O}).



As already remarked, the results show that in all cases the electrochemical reaction occurs mostly in the AL (Figure 4a), with the SL providing mainly a path for the electronic current from the AL to the current collector, while accomplishing its primary function of mechanical support for the whole fuel cell. In our simulations, the composition of the SL is within the percolation thresholds of both Ni and YSZ, so that, in principle, some electrochemical reaction might occur also in the SL. Indeed, our simulations show that this actually takes place for the AL composition 2_b ($\phi_{el,AL} = 0.34$), within the first 20–30 μm of SL thickness adjacent to the AL, while, for the other AL compositions, practically no electrochemical reaction occurs in the SL (the simulated EAT values are reported in Table 3). This latter result is due to the fact that at typical IT-SOFC operating temperatures (here, 1073 K) the bulk YSZ ionic resistivity is of the order of $\approx 5 \times 10^{-3} \Omega \cdot \text{cm}$ (from the data in Table 2, [40]), which is several orders of magnitude higher than the bulk Ni electronic resistivity ($\approx 5 \times 10^{-9} \Omega \cdot \text{cm}$, Table 2). As a consequence, the oxygen ions entering the AL, face a very high resistance in their path along the ionic conductor, and this forces them to react electrochemically with hydrogen (Equation (4)) within a short thickness of the AL. In the light of these considerations, the lower the effective ionic resistivity of the AL, the thicker the layer where the electrochemical reaction takes place, which might eventually lead to an extension of the electrochemical reaction into the SL. In turn, as already remarked in Section 2, the effective ionic resistivity of the AL strongly depends on its YSZ content, and it is lower for high YSZ volumetric fractions (corresponding to low Ni volumetric fraction: Case 2_b , where $\phi_{el} = 0.34$, is about 10% above the Ni percolation threshold).

Table 3. Simulated $1/R_p$, electrochemically active thickness (EAT) and effective electronic and ionic resistivities of the AL, for three different Ni-YSZ compositions, at 1073 K.

AL	2_b	2_c	2_d
$\phi_{el,AL}$ (-)	0.34	0.44	0.55
$\rho_{io,AL}^{eff}$ ($\Omega \cdot \text{cm}$)	156	294	856
$\rho_{el,AL}^{eff}$ ($\Omega \cdot \text{cm}$)	0.02	2.3×10^{-3}	7.6×10^{-4}
EAT (μm)	26	16	9
$1/R_p$ ($\text{S} \cdot \text{cm}^{-2}$)	5.97	5.18	3.34

The results reported in Table 3 show that there is a correlation between the effective ionic resistivity $\rho_{io,AL}^{eff}$ of the AL, the EAT and the electrode $1/R_p$ in the range of AL compositions taken into consideration (2_b – 2_d): the lower $\rho_{io,AL}^{eff}$, the larger the EAT and $1/R_p$. This finding is in agreement with the results reported by [36] for single-layer SOFC electrodes. However, Figure 2 shows that a further reduction of Ni content of the AL below that of Case 2_b , leads to a decreased $1/R_p$. In this latter case, the effective ionic conductivity increases over that of Case 2_b , but a significant reduction of the active area A available for the electrochemical reaction (which tends to zero at the percolation thresholds) occurs, increasing activation losses and decreasing $1/R_p$. Thus, the correlation between the effective ionic resistivity $\rho_{io,AL}^{eff}$ of the AL and the electrode $1/R_p$ demonstrated by Table 3, does not hold for compositions very close to the percolation thresholds.

The profile of electrode overpotential η , displayed in Figure 4b,c, is qualitatively similar in Cases 2_c and 2_d , while a slightly different behavior is reported for Composition 2_b . Indeed, Figure 4b shows that, for Compositions 2_c and 2_d , the profile of overpotential η at the AL/SL interface does not

change slope (*i.e.*, the first order derivative of η is continuous), while for Composition 2_b, a change in slope is visible (*i.e.*, the first order derivative of η has a discontinuity). From a mathematical (and physical) point of view, this is due to the boundary conditions at the AL/SL boundary (Equation (11)): the electronic and ionic currents i_{el} and i_{io} must be unchanged across the AL/SL boundary. The derivative of η , which is (from Equation (1)):

$$\frac{d\eta}{dy} = \rho_{io}^{eff} i_{io} - \rho_{el}^{eff} i_{el} \quad (14)$$

is, thus, discontinuous across the AL/SL interface, due to the change in morphology and, thus, in effective resistivity ρ_{io}^{eff} and ρ_{el}^{eff} from the AL to the SL. In Cases 2_c and 2_d, being i_{io} close to zero at the AL/SL interface, and also being ρ_{el}^{eff} very small in both the AL and SL layers, the slope of the curve representing η in Figure 4b is close to zero as well, and no change of slope is visible across the AL/SL interface. On the contrary, in Case 2_b, as already remarked, a relevant part of the electrochemical reaction takes place within the SL, and i_{io} is significant at the AL/SL interface. Thus, the change in ionic resistivity ρ_{io}^{eff} across the AL/SL interface results in a marked discontinuity of the slope of η .

Additionally, Figure 4b shows that in Case 2_b, the extension of the *EAL* into the electrode thickness is related to a smoother profile of η compared to the other Cases 2_c and 2_d. In turn, this is related to a lower value of the overall electrode overpotential η_{tot} and to the already discussed higher value of $1/R_p$.

Figure 4c shows that, in all cases, the overpotentials vary linearly in the SL, since here, as already discussed, only ohmic electronic conduction along the percolating clusters of Ni particles occurs. Figure 4c shows that, in the SL, η values are not completely negligible; however, the related electrochemical reaction rate is negligible, since the active area for the electrochemical reaction A is very small due to the relatively large size of the particles employed in the SL ($r = 0.5 \mu\text{m}$). As already remarked in the discussion of Figure 4a, the electrochemical reaction rate is significant only in the AL, where values of η in the range 0.03–0.16 V, are associated to a large active area A due to the small size of the AL particles ($r = 0.25 \mu\text{m}$).

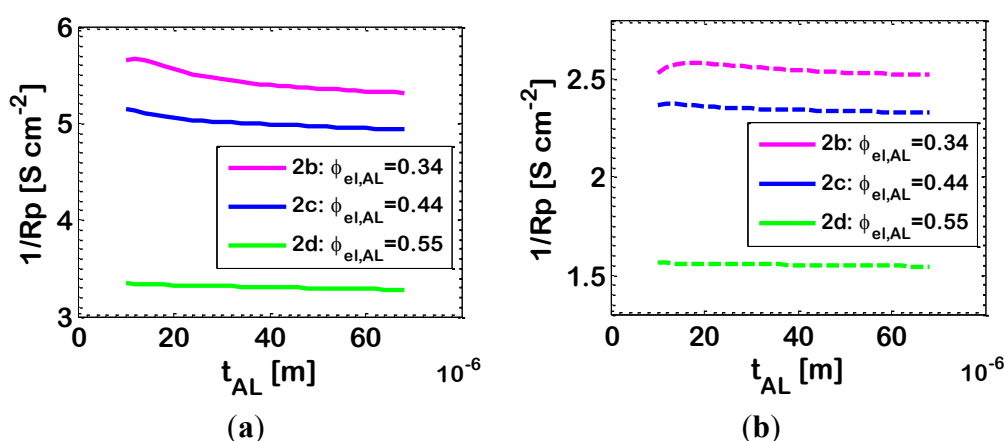
Profiles of hydrogen/water partial pressure in Cases 2_b, 2_c and 2_d are reported Figure 4c, showing again practically identical results in Cases 2_c and 2_d, and a different behavior in Case 2_b. Again, the difference is explained considering that in Cases 2_c and 2_d the electrochemical reaction occurs mostly in the AL, while in Case 2_b it is shifted towards the SL. In addition, it must be kept in mind that the AL has smaller particles, and thus smaller pores (Equation (7)) than the SL, resulting in slower diffusion (Knudsen diffusivity is the limiting diffusivity in the AL). As a result, if the electrochemical reaction occurs close to the AL/electrolyte interface (Cases 2_c and 2_d), then the water generated by the electrochemical reaction tends to remain entrapped into the AL itself, hindering also the access to hydrogen. On the contrary, if the electrochemical reaction is shifted towards the AL/SL interface, or even into the SL (Case 2_b), then diffusion of water and hydrogen to/from the SL/current collector (=gas distributor) interface is expedited. This is the reason why, in Cases 2_c and 2_d, the partial pressure of water (p_{H_2O}) in the AL is higher than in Case 2_b and, symmetrically, the partial pressure of hydrogen (p_{H_2}) is lower. Figure 4c shows that this holds also for the SL. As a final remark, in the SL, for $30 \mu\text{m} < y < 710 \mu\text{m}$, the fluxes of hydrogen and water are identical in all the three cases, because they are associated to the overall current density I_{tot} , which is the same. These identical fluxes are related to different profiles of hydrogen and water partial pressures

(Figure 4c), and this is explained by considering that diffusivities are different as well, since Knudsen diffusivities have an impact also in the SL, and H_2 and H_2O Knudsen diffusivities are different from each other ($D_{H_2,K}^{eff} = 3D_{H_2O,K}^{eff}$). Thus, in Case 2_b, where the partial pressure of water (p_{H_2O}) is the lowest and, symmetrically, the partial pressure of hydrogen (p_{H_2}) is the highest, the effective diffusivity of the gaseous mixture is the highest, and the partial pressure profiles are flatter (Equation (6)).

3.4. Effect of Active Layer Thickness

Considering bi-layer electrodes with the characteristics reported in Table 2, Figure 5 shows simulation results investigating the effect of an increase of the AL thickness above 10 μm (ALs with thickness below 10 μm have received little attention from an experimental point of view). In principle, an increase of the AL thickness is expected to affect adversely the various sources of loss. Ohmic and diffusive losses are expected to increase due to an increase of the length of the charge conducting and gas diffusion paths. On the contrary, activation losses are expected to decrease due to an extension of the thickness available for the electrochemical reaction. The effect of an increase of the AL above values of 10 μm , up to 50–60 μm , was investigated experimentally by several literature studies. Some experimental results from the literature, obtained from the EIS technique [52], report no influence from this parameter, and explain this effect as a consequence of a compensation between reduced activation losses and increased diffusive losses. Our simulation results are displayed in Figure 5 for the three AL Compositions 2_b, 2_c and 2_d, defined in Figure 2. In particular, Figure 5 displays a well visible plateau for composition 2_d ($\phi_{el,AL} = 0.55$), which agrees qualitatively well with the literature experimental data discussed above.

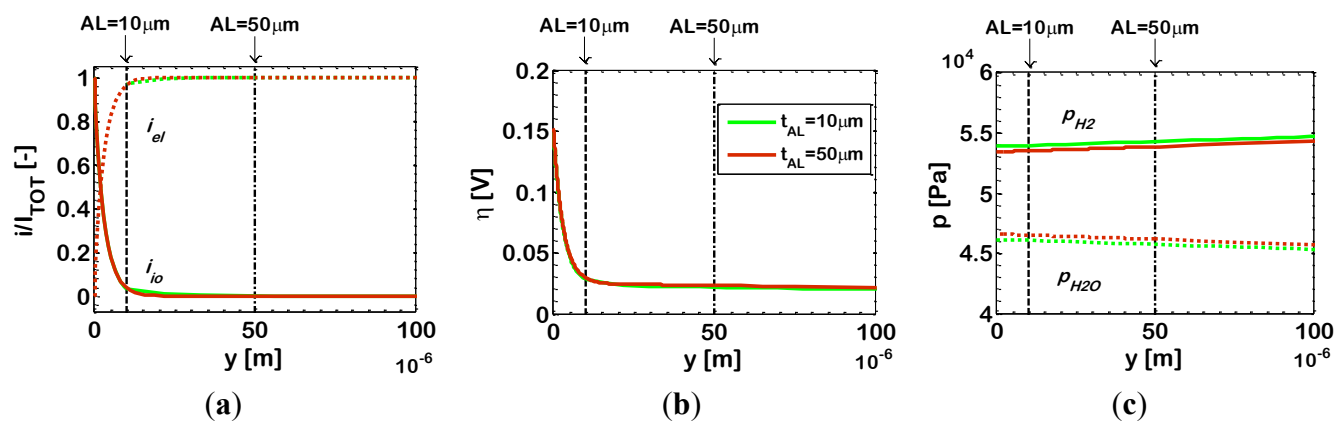
Figure 5. Effect of AL thickness on the $1/R_p$ of bi-layered Ni-YSZ anodes (data in Table 2). Varying parameter: Ni volumetric fraction in the AL ($\phi_{el,AL}$). Simulations at temperature: (a) $T = 1073$ K; and (b) $T = 973$ K.



In order to investigate further this behavior, in Figure 6 we report the simulated distributions of dimensionless current density i/I_{tot} , overpotential η and partial pressures of hydrogen (p_{H_2}) and water (p_{H_2O}) along the electrode thickness for two different bi-layered electrodes with different AL thicknesses (10 μm and 50 μm), with $\phi_{el,AL} = 0.55$ and operating at $T = 1073$ K. The results for $t_{AL} = 10$ μm and 50 μm are plotted in the same figures, and in both cases the y co-ordinate has its origin located at the AL/electrolyte interface.

Figure 6a displays an enlargement of the AL, showing that, for both ALs (10 μm and 50 μm), the distributions of current density i/I_{tot} are superimposed; the EAT is the same, *i.e.*, about 9 μm adjacent to the E/E interface. Indeed, as already remarked, the width of the EAT is related to the effective ionic resistivity $\rho_{\text{io}}^{\text{eff}}$ of the AL, and an increase of the AL thickness does not bring any changes: it is only an additional AL portion where conduction of electrons on the Ni clusters occurs with no electrochemical reaction. We also investigate the distributions of hydrogen and water partial pressures, which again are very close to each other with both the ALs under consideration (Figure 6c). The results show just a slightly lower p_{H_2} and higher $p_{\text{H}_2\text{O}}$ in the case of 50 μm AL, explained by the increased diffusion length. In this scenario, obviously also the distribution of the overpotential η along the electrode thickness is the same for both ALs (10 μm and 50 μm), which is reported in Figure 6b, and also the value of $1/R_p$ is the same, as displayed in Figure 5.

Figure 6. Bi-layered Ni-YSZ anodes at temperature $T = 1073$ K; Ni volumetric fraction in the AL $\phi_{\text{el,AL}} = 0.55$ (Case 2_d). Other data reported in Table 2. Varying parameter: AL thicknesses: $t_{\text{AL}} = 10$ μm and 50 μm . Simulated distributions along the electrode thickness of: (a) ionic (i_{io}) and electronic (i_{el}) currents; (b) overpotential (η); and (c) partial pressures of hydrogen (p_{H_2}) and water ($p_{\text{H}_2\text{O}}$).



Thus, our simulation results for $\phi_{\text{el,AL}} = 0.55$ are in agreement with literature data reporting that an increase of the AL thickness over 10 μm is practically non-influential, but the explanation we propose for this behavior is different from that reported in the literature, since simulation results show that increase of the AL thickness does not modify any of the sources of losses, neither activation nor diffusive.

The literature reports also slightly different results for electrodes with different characteristics. For example, some literature studies [54], based on the experimental evaluation of V - I characteristic curves of full scale IT-SOFCs deploying bi-layer anodes, demonstrate a decrease of the overall anode $1/R_p$ when increasing the anode AL thickness, and this is explained as a result of diffusive losses being more sensitive to a variation of the AL thickness than the other sources of losses. This is captured, in our simulations, in a qualitative manner, by the results displayed in Figure 5 by the curves for Composition 2_c ($\phi_{\text{el,AL}} = 0.44$), which show a slight decrease of $1/R_p$ when increasing the anode AL thickness. Actually, in this case, the slight increase of diffusion limitations by increasing the AL thickness, demonstrated in Figure 6c, becomes more effective.

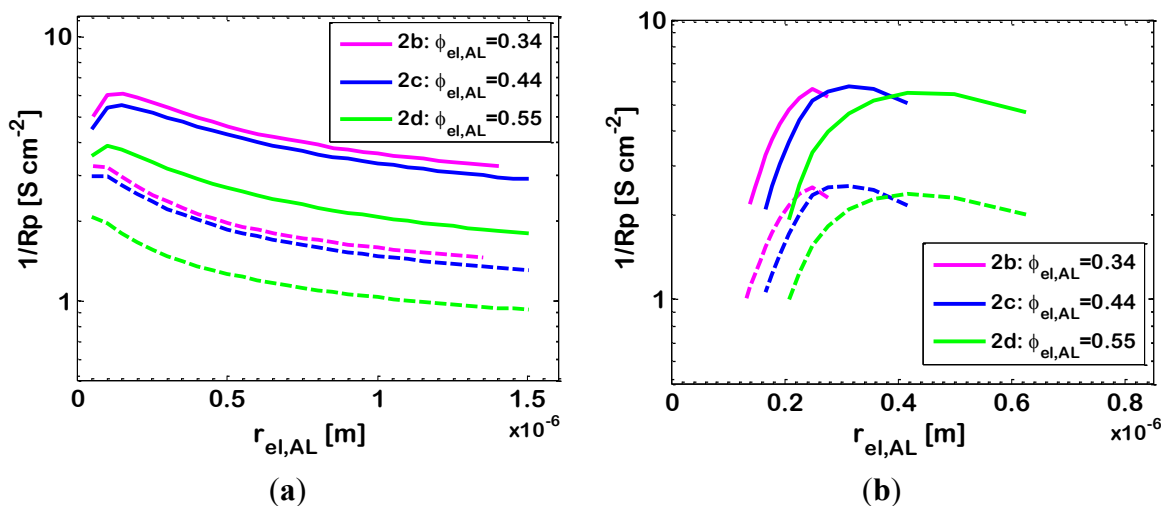
Further, some other literature works [18,56] report for $1/R_p$ an increase up to AL thicknesses in the order of 15 μm , followed by a decrease. This is consistent with experimental literature data for single-layer HT-SOFC electrodes [57], and is captured, in our simulations, by the results in Figure 5, curves with $\phi_{\text{el,AL}} = 0.34$ (Case 2_b), which show a maximum for an AL thicknesses in the order of 15 μm . Here, the scenario is slightly different, because the ionic conductivity of the AL is more than five times higher than in the case with $\phi_{\text{el,AL}} = 0.55$, and thus the EAT is significantly larger (26 μm , from Table 3). As a consequence, an increase of the thickness of the AL from 10 μm to 15 μm brings an improvement of the electrode microstructure, and thus increases of the active area available for the electrochemical reaction A , exactly where the major part of the electrochemical reaction takes place, and this leads to an increase of $1/R_p$. In Figure 5, the decrease displayed by the simulation results for $t_{\text{AL}} > 15 \mu\text{m}$, is due, again, to an increase of diffusion limitations.

3.5. Effect of Active Layer Particle Dimensions

Usually, AL particles are quite small (Table 1), because this region is devoted to the electrochemical reaction, which is enhanced in presence of a large active area A , which is obtained with small particles rather than with large ones.

In a first simulation, we analyze the electrode behavior with AL particle radii in the range 0.1–1.5 μm , considering the ionic and electronic particle radii identical ($P = \frac{r_{\text{io}}}{r_{\text{el}}} = 1$). Simulations are run at temperatures $T = 973 \text{ K}$ and 1073 K ; all the other parameters have the values reported in Table 2. The simulation results are reported in Figure 7a, which shows a maximum of $1/R_p$ for particle radii of 0.2–0.3 μm , which is a trade-off between the effect of diffusive losses (which are relevant for particles with radius smaller than 0.1–0.2 μm : the smaller the particles, the smaller the AL pores, which decreases Knudsen diffusivities) and activation losses (which are relevant for large particle radii, since the active area for the electrochemical reaction A is reduced).

Figure 7. Effect of AL Ni particle radius $r_{\text{el,AL}}$ on the $1/R_p$ of bi-layered Ni-YSZ anodes. Temperatures: $T = 973 \text{ K}$ (dashed lines) and $T = 1073 \text{ K}$ (solid lines); other data in Table 2. Varying parameter: Ni volumetric fraction in the AL ($\phi_{\text{el,AL}}$). Simulations results: (a) r_{io} is varied together with r_{el} so that $r_{\text{io}} = r_{\text{el}}$ ($p = 1$); and (b) r_{io} is kept at the constant value of 0.25 μm through all the simulations.



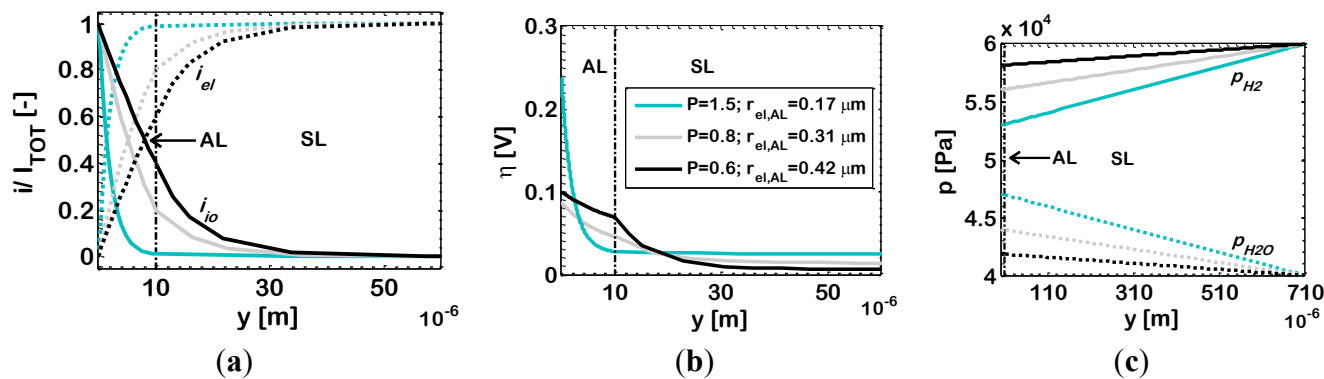
We also investigate the case where the ionic and electronic conducting particles of the AL have different size. In particular, we analyze the effect of employing Ni particles of various radii in the range 0.1–0.7 μm , by keeping the YSZ particle radius at 0.25 μm . The simulation results are reported in Figure 7b, and, again, show a maximum. For a further investigation of this behaviour, in Figure 8 we draw the simulated distributions of dimensionless current density i/I_{tot} , overpotential η and partial pressures of hydrogen (p_{H_2}) and water ($p_{\text{H}_2\text{O}}$) along the electrode thickness for an anode with $\phi_{\text{el,AL}} = 0.44$ (Case 2c), $T = 1073$ K and for three different Ni radii: $r_{\text{el}} = 0.17$, 0.31 and 0.42 μm , corresponding to $P = 1.5$, 0.8 and 0.6, respectively. In this case, a change in the Ni particle radius r_{el} , results in a change of P and also in a change of the percolation thresholds of both Ni and YSZ; in a binary mixture of bi-modal particles, the larger particles require a higher volume fraction to percolate. In the light of this, we discuss Figure 8 by considering, at first, the results reported for $r_{\text{el}} = 0.17$ μm ($P = 1.5$). Here, the YSZ particles are larger than the Ni ones, and the percolation thresholds are about $\phi_{\text{el}} = 0.23$ and $\phi_{\text{el}} = 0.62$ (*i.e.*, $\phi_{\text{io}} = 0.38$) for the electronic and ionic conductors, respectively. Thus, the electrode under analysis, with $\phi_{\text{el,AL}} = 0.44$, has an ionic volumetric fraction which is quite far from the electronic percolation threshold, and, thus, its effective ionic resistivity is quite high (about $2.15 \times 10^3 \Omega \cdot \text{cm}$, simulation result). As a consequence, as displayed by Figure 8a, the length of penetration of the electrochemical reaction inside the AL is not very high (EAT ≈ 6 μm , simulation result). Thus, the overpotential η is high (Figure 8b), as well as η_{tot} , and the value of $1/R_p$ is low (Figure 7b). The low value of $1/R_p$ is also explained by the fact that here the particles are rather small, and thus the electrode pores are small as well, causing significant diffusion limitations, as displayed by Figure 8c which shows high values of $p_{\text{H}_2\text{O}}$ and low values of p_{H_2} in the AL. If now we consider $r_{\text{el}} = 0.31$ μm , P is decreased to 0.8, the percolation thresholds move to about $\phi_{\text{el}} = 0.33$ and $\phi_{\text{el}} = 0.74$ (*i.e.*, $\phi_{\text{io}} = 0.26$) for the electronic and ionic conductors respectively, and thus our $\phi_{\text{el}} = 0.44$ is closer to the percolation threshold of the electronic conductor, resulting in a higher ionic conductivity. As a consequence, Figure 8a shows that the penetration of the electrochemical reaction inside the electrode thickness is higher, reaching the SL and displaying some electrochemical reaction occurring even in the SL (EAT ≈ 28 μm). This increased penetration of the electrochemical reaction leads to a lower value of η (principally at the AL/electrolyte interface, Figure 8b) and of η_{tot} , and finally to a higher value of $1/R_p$.

Finally, if r_{el} is further increased to 0.42 μm (corresponding to $P = 0.6$), the percolation thresholds move to about $\phi_{\text{el}} = 0.42$ and $\phi_{\text{el}} = 0.80$ (*i.e.*, $\phi_{\text{io}} = 0.20$) for the electronic and ionic conductors, respectively, and thus our $\phi_{\text{el,AL}} = 0.44$ is now very close to the percolation threshold of the electronic conductor, resulting in a further increased ionic conductivity. Figure 8a shows that the penetration of the electrochemical reaction inside the electrode thickness increases again (EAT ≈ 33 μm), but the value of η is now slightly increased, compared to the previous case (principally at the AL/electrolyte interface, Figure 8b). As already remarked, this is due to the fact that, since we are getting very close to one of the percolation thresholds, another effect becomes important, *i.e.*, the active area per unit volume A is reduced, and this explains the higher value of η , which leads to a higher value of η_{tot} and finally to a lower value of $1/R_p$ compared to the previous case.

Concerning the partial pressure profiles reported in Figure 8c, our simulation results show again that, if we compare the case where the electrochemical reaction occurs close to the AL/electrolyte interface, to the case where the electrochemical reaction is shifted towards the AL/SL interface or even inside the SL,

then in the previous case: (i) the partial pressure of water (p_{H_2O}) in the AL is higher; (ii) symmetrically, the partial pressure of hydrogen (p_{H_2}) is lower; and (iii) the profiles of partial pressures in the SL are steeper.

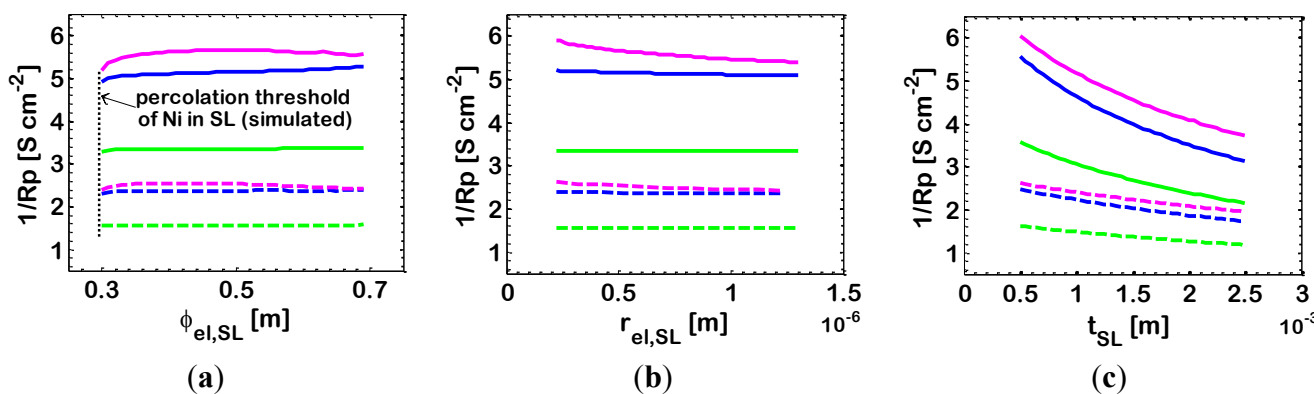
Figure 8. Bi-layered Ni-YSZ anodes at temperature $T = 1073$ K; Ni volumetric fraction in the AL $\phi_{el,AL} = 0.44$ (Case 2_c). Other data reported in Table 2. Varying parameter: AL Ni particle radius $r_{el,AL}$. Simulated distributions along the electrode thickness of: (a) ionic (i_{io}) and electronic (i_{el}) currents; (b) overpotential (η); and (c) partial pressures of hydrogen (p_{H_2}) and water (p_{H_2O}).



3.6. Effect of Support Layer Characteristics

The effect of the characteristics of the SL on the electrode $1/R_p$ are presented in Figure 9. In these simulations the parameters of the AL are kept at the values reported in Table 2.

Figure 9. Effect of SL characteristics on the $1/R_p$ of bi-layered Ni-YSZ anodes operating at temperatures: $T = 973$ K (dashed lines) and $T = 1073$ K (solid lines). Other data are reported in Table 2. Varying parameter: Ni volumetric fraction in the AL: — Case 2_b ($\phi_{el,AL} = 0.34$); — Case 2_c ($\phi_{el,AL} = 0.44$); and — Case 2_d ($\phi_{el,AL} = 0.55$). Simulations results of the impact of: (a) SL Ni volumetric fraction ($\phi_{el,SL}$); (b) SL particle dimensions ($r_{el,SL} = r_{io,SL}$); and (c) SL thickness (t_{SL}).



In principle, it is not strictly necessary for the YSZ phase to percolate through the SL, because the main electrochemical role of the SL is to provide a path for the electrons from the AL to the current collector. However, as already discussed, the presence YSZ particles into the SL, above the percolation threshold, is beneficial from the point of view of the electrochemical performance,

allowing a possible extension of the electrochemical reaction also into the SL. In addition, the presence of YSZ into the SL avoids Ni agglomeration and ensures that the TEC is as close as possible to that of the AL [24]. Due to the importance of this last issue, the Ni content of the SL is usually around 50%, and in some cases another additional layer is introduced between the AL and the SL [58,59], which allows a smoother transition.

On the basis of our simulation model, we investigate the effect of Ni volumetric fraction ($\phi_{el,SL}$), particle dimensions ($r_{el,SL}$) and thickness (t_{SL}) of the SL. Figure 9a shows that the effect of a variation of the SL Ni content is related to the AL characteristics. Indeed, if we are in a case where the electrochemical reaction does not occur entirely in the AL, but is shifted towards the AL/SL interface and occurs also in part in the SL, then the characteristics of the SL impact the overall electrode electrochemical performance. In particular, Figure 9a shows that, for $\phi_{el,AL} = 0.34$ (Case 2_b), the electrode $1/R_p$ is maximum for $\phi_{el,SL} = 0.5$. On the contrary, Figure 9a shows that if the electrochemical reactions occurs entirely in the AL, for $\phi_{el,AL} = 0.44$ (Case 2_c) and $\phi_{el,AL} = 0.55$ (Case 2_d), then there is no influence of the SL Ni content on the overall electrode electrochemical performance.

Analogously, Figure 9b shows the effect of a variation of the radius of the SL particles in the range of 0.25–1.2 μm (keeping identical the dimensions of the ionic and electronic particles: $P = \frac{r_{io}}{r_{el}} = 1$). Radii in the order of 0.5–1 μm are reported in the literature [60]. More in detail, Figure 9b shows a slight decrease of electrode performance with increasing the size of the SL particles. Again, this effect is visible only in the case where the properties of the AL allow the electrochemical reaction to occur in part in the SL ($\phi_{el,AL} = 0.34$, Case 2_b). Here, the increase of the SL particle dimensions reduces the active area A for the SL electrochemical reaction in the SL, and this decreases the overall electrode $1/R_p$. This effect, of course, is not visible for $\phi_{el,AL} = 0.44$ (Case 2_c) and $\phi_{el,AL} = 0.55$ (Case 2_d), where the electrochemical reaction occurs almost entirely in the AL. Concerning a possible impact on diffusive losses we remark that, at 1073 K, with SL particle radii larger than about 1 μm , pores (Equation (7)) are large enough to be practically outside the Knudsen regimen at the operating temperatures under consideration, which means that diffusivity values are typical of molecular diffusivity, which is independent of pore radius. Likewise, also a variation of the radius of SL Ni particles in the range of 0.25–1 μm has a minor impact on diffusive losses.

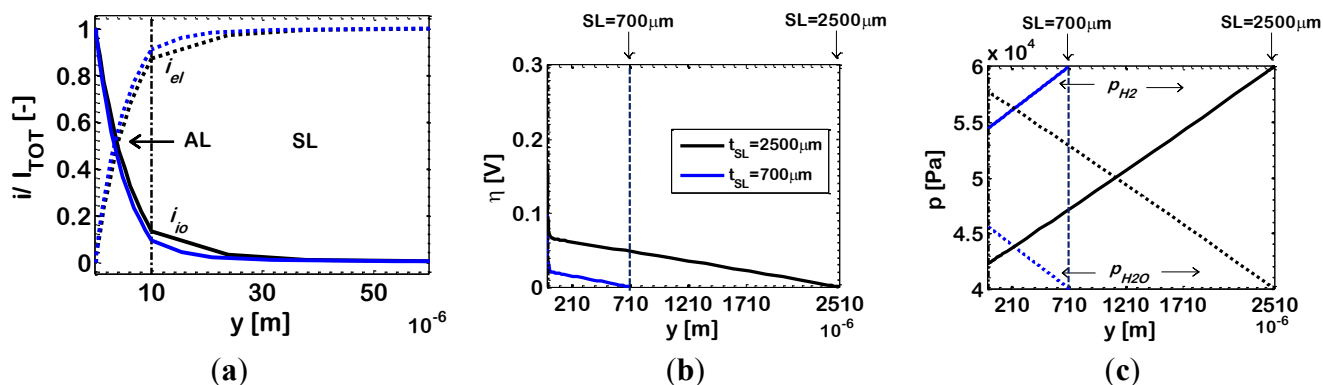
Finally, Figure 9c shows the negative effect of an increase of the SL thickness t_{SL} from 700 μm to 2500 μm , demonstrating that this is expected to lead to a decrease of the electrode $1/R_p$ of about 30%.

For a further investigation of this result, in Figure 10 we draw the simulated distributions of dimensionless current density i/I_{tot} , overpotential η and partial pressures of hydrogen (p_{H_2}) and water (p_{H_2O}) along the electrode thickness for $\phi_{el,AL} = 0.44$ (Case 2_c) and for two different SL thicknesses (700 μm and 2500 μm). The results for $t_{SL} = 700 \mu\text{m}$ and 2500 μm are plotted on the same figures, and in both cases the y co-ordinate has its origin at the AL/electrolyte interface.

Figure 10a shows that the penetration of the electrochemical reaction inside the electrode does not change significantly by increasing the SL thickness (EAT $\approx 16 \mu\text{m}$ with $t_{SL} = 700 \mu\text{m}$; EAT $\approx 21 \mu\text{m}$ with $t_{SL} = 2500 \mu\text{m}$). On the contrary, by increasing the SL thickness there is an increase in the length of the diffusion path through which hydrogen and water must migrate in the SL, which leads to lower hydrogen and higher water concentrations in the AL (Figure 10c), with a consequent decrease of

the electrochemical kinetics (Equation (1)), resulting thus in an increased η in the AL (Figure 10b), which finally leads to a lower $1/R_p$ value.

Figure 10. Bi-layered Ni-YSZ anodes at temperature $T = 1073$ K; Ni volumetric fraction in the AL $\phi_{el,AL} = 0.44$ (Case 2_c). Other data reported in Table 2. Varying parameter: SL thickness (t_{SL}). Simulated distributions along the electrode thickness of: (a) ionic (i_{i0}) and electronic (i_{el}) currents; (b) overpotential (η); and (c) partial pressures of hydrogen (p_{H_2}) and water (p_{H_2O}).



Even if our results suggest that bi-layered electrodes with thin SL display better electrochemical performance, nevertheless, the choice of geometrical and morphological parameters of the SL must be made taking into account not only the electrode electrochemical performance, but also the desired mechanical features. In this sense, a thickness as high as 0.7–1.5 mm is often reported for SLs of bi-layered IT-SOFC anodes [61,62]. Cathode thicknesses as high as 2.2 mm were adopted for tubular cathode-supported HT-SOFCs [3], in order to ensure adequate mechanical stability.

4. Conclusions

We consider IT-SOFC Ni-YSZ bi-layered anodes composed by an AL adjacent to the electrolyte, coupled to a SL adjacent to the current collector/gas distributor. The aim of this configuration is to obtain anodes able to act as a support for the whole IT-SOFC, coupling the high electrochemical performance of thin composite electrodes formed by small particles, to the high mechanical strength of thick layers formed by large particles. This type of electrodes has recently been widely investigated from an experimental point of view, drawing interesting conclusions about the relative importance of diffusion, ohmic, and activation losses. In the present work, our aim is to investigate these electrodes from a modeling perspective. Our simulation addresses an electrode formed by a 10 μm thick AL formed by 0.25 μm radius Ni and YSZ particles. The AL is coupled to a 700 μm thick SL formed by 0.5 μm radius Ni and YSZ particles. Simulation results of the overall electrode resistance (taking into account diffusion, ohmic and activation losses at the same time) are in good agreement with literature experimental data. Our model allows to calculate ionic and electronic currents, as well as overpotentials and reactant partial pressures along the electrode thickness. Simulation results show that the electrochemical reaction takes place mostly in the AL with seldom penetration into a 20–30 μm width of the adjacent SL. Thus, the characteristics of the AL dominate the electrochemical performance of the electrode, and in particular, percolation of both the electronic and ionic conducting particles plays a

key role. In addition, increased penetration of the electrochemical reaction into the electrode thickness is obtained at high YSZ content, *i.e.*, low Ni content of the AL. Simulation results show that, with a Ni content of the AL about 10% higher than its percolation threshold, the overall anode electrochemical performance is significantly enhanced, and this is confirmed also by literature experimental data.

Modeling results show that the morphology of the SL, in particular the particle radius, has a minor effect on the electrochemical performance of the electrode, and thus this can be suitably tailored in order to optimize the mechanical features, which usually addresses the choice towards relatively large particles (radius ranging between 0.25 μm and 1.5 μm). Concerning the Ni content of the SL, the simulation results show that a Ni content of 50% is beneficial, in some cases, in order to improve the electrode electrochemical performance. This choice of composition is frequently reported by literature experimental studies because it is also expected to avoid Ni agglomeration issues thanks to the high YSZ content, and also to ensure a TEC as close as possible to that of the AL. Modeling results also show that an increase of the thickness of the SL impacts negatively the electrode electrochemical performance, due to increased diffusion limitations. Nevertheless, the need to meet the mechanical requirements addresses the choice towards a sufficiently thick support, even if simulation results indicate that doubling the thickness of the SL from 700 μm to 1400 μm leads to a 20% increase of the overall electrode resistance.

Acknowledgments

We wish to thank Laura Bisio and Elena Sala for fruitful discussions during this work.

Notation

A	active area per unit volume ($\text{cm}^2 \cdot \text{cm}^{-3}$)
D	diffusivity ($\text{cm}^2 \cdot \text{s}^{-1}$)
F	Faraday's constant ($96487 \text{ C} \cdot \text{mol}^{-1}$)
i	current density ($\text{A} \cdot \text{cm}^{-2}$)
i_0	exchange current density ($\text{A} \cdot \text{cm}^{-2}$)
i_n	transfer current density per unit of active area ($\text{A} \cdot \text{cm}^{-2}$)
I_{tot}	overall electrode current density ($\text{A} \cdot \text{cm}^{-2}$)
N	molar flux of the component i ($\text{mol} \cdot \text{cm}^{-2} \cdot \text{s}^{-1}$)
p_i	partial pressure of i component (atm)
P	particles dimension ratio (r_{i0}/r_{el})
r	particle radius (cm)
R	universal gas constant ($\text{J} \cdot \text{mol}^{-1} \cdot \text{K}^{-1}$)
R_p	overall electrode specific resistance ($\Omega \cdot \text{cm}^2$)
r_{pore}	mean pore radius (cm)
t	layer thickness (cm)
T	temperature (K)
V	electric potential (V)
y	model coordinate (cm)
x_i	molar fraction (of i component)

Greek Symbols

β	transfer coefficient
ε	porosity
η	overpotential (V)
ρ	resistivity (ohm cm)
τ	tortuosity
ϕ	volumetric fraction

Subscript

AL	active layer
el	electronic
io	Ionic
K	Knudsen
SL	support layer

Superscript

0	inlet
eff	effective

Acronyms

AL	active layer
EAT	electrochemically active thickness
E/CC	electrode/current-collector
E/E	electrode/electrolyte
EIS	electrochemical impedance spectroscopy
FGE	functionally graded electrode
HT-SOFC	high temperature-solid oxide fuel cell
IT-SOFC	intermediate temperature-solid oxide fuel cell
LSGM	$\text{La}_x\text{Sr}_{1-x}\text{Ga}_y\text{Mg}_{1-y}$
SL	support layer
SOFC	solid oxide fuel cell
TPB	three-phase boundary
TEC	thermal expansion coefficient
YSZ	$(\text{ZrO}_2)_x(\text{Y}_2\text{O}_3)_{1-x}$

Conflicts of Interest

The authors declare no conflict of interest.

References

1. Singhal, S.C. Advances in solid oxide fuel cell technology. *Solid State Ion.* **2000**, *135*, 305–313.
2. Appleby, A.J. Fuel Cells—Overview: Introduction. In *Encyclopedia of Electrochemical Power Sources*; Elsevier: Oxford, UK, 2009; pp. 277–296.
3. Singhal, S.C.; Kendall, K. *High Temperature Solid Oxide Fuel Cells: Fundamentals, Design and Applications*; Elsevier Advanced Technology: Oxford, UK, 2003.
4. Steele, B.C.H. Materials for IT-SOFC stacks 35 years R&D: The inevitability of gradualness? *Solid State Ion.* **2000**, *134*, 3–20.
5. Shirazi, A.; Aminyavari, M.; Najafi, B.; Rinaldi, F.; Razaghi, M. Thermal-economic-environmental analysis and multi-objective optimization of an internal-reforming solid oxide fuel cell-gas turbine hybrid system. *Int. J. Hydrog. Energy* **2012**, *37*, 19111–19124.
6. Najafi, B.; Shirazi, A.; Aminyavari, M.; Rinaldi, F.; Taylor, R.A. Exergetic, economic and environmental analyses and multi-objective optimization of an SOFC-gas turbine hybrid cycle coupled with an MSF desalination system. *Desalination* **2014**, *334*, 46–59.
7. Shao, Z.; Zhou, W.; Zhu, Z. Advanced synthesis of materials for intermediate-temperature solid oxide fuel cells. *Prog. Mater. Sci.* **2012**, *57*, 804–874.
8. Liu, M.; Lynch, M.E.; Blinn, K.; Alamgir, F.M.; Choi, Y. Rational SOFC material design: New advances and tools. *Mater. Today* **2011**, *14*, 534–546.
9. Zhao, F.; Virkar, A.V.J. Dependence of polarization in anode-supported solid oxide fuel cells on various parameters. *J. Power Sources* **2005**, *141*, 79–95.
10. Moon, H.; Kim, S.D.; Hyun, S.H.; Kim, H.S. Development of IT-SOFC unit cells with anode-supported thin electrolytes via tape casting and co-firing. *Int. J. Hydrog. Energy* **2008**, *33*, 1758–1768.
11. Song, J.H.; Park, S.I.; Lee, J.H.; Kim, H.S. Fabrication characteristic of an anode-supported thin-film electrolyte by tape-casting method for IT-SOFC. *J. Mater. Process. Technol.* **2008**, *198*, 414–418.
12. Timurkutluk, B.; Mat, M.D. Effects of anode fabrication parameters on the performance and redox behavior of solid oxide fuel cells. *J. Power Sources* **2014**, *258*, 108–116.
13. Han, M.F.; Yin, H.Y.; Miao, W.T.; Zhou, S. Fabrication and properties of anode-supported solid oxide fuel cell. *Solid State Ion.* **2008**, *179*, 1545–1548.
14. Biswas, S.; Nithyanantham, T.; Thangavel, S.N.; Bandopadhyay, S. High-temperature mechanical properties of reduced NiO-8YSZ anode-supported bi-layer SOFC structures in ambient air and reducing environments. *Ceram. Int.* **2013**, *39*, 3103–3111.
15. Brown, M.; Primdahl, S.; Mogensen, M. Structure/performance relations for Ni/yttria-stabilized zirconia anodes for solid oxide fuel cells. *J. Electrochem. Soc.* **2000**, *147*, 475–485.
16. Cannarozzo, M.; Grosso, S.; Agnew, G.; del Borghi, A.; Costamagna, P. Effects of mass transport on the performance of solid oxide fuel cells composite electrodes. *J. Fuel Cell Sci. Technol.* **2007**, *4*, 99–106.
17. Müller, A.C.; Herbstritt, D.; Ivers-Tiffée, E. Development of a multilayer anode for solid oxide fuel cells. *Solid State Ion.* **2002**, *152–153*, 537–542.

18. Yoon, D.; Lee, J.-J.; Park, H.-G.; Hyun, S.-H. NiO/YSZ-YSZ nanocomposite functional layer for high performance solid oxide fuel cell anodes. *J. Electrochem. Soc.* **2010**, *157*, B455–B462.
19. Lee, K.T.; Yoon, H.S.; Wachsman, E.D. The evolution of low temperature solid oxide fuel cells. *J. Mater. Res.* **2012**, *27*, 2063–2078.
20. Hanna, J.; Lee, W.Y.; Shi, Y.; Ghoniem, A.F. Fundamentals of electro- and thermochemistry in the anode of solid-oxide fuel cells with hydrocarbon and syngas fuels. *Prog. Energy Combust. Sci.* **2014**, *40*, 74–111.
21. Atkinson, A.; Barnett, S.; Gorte, R.J.; Irvine, J.T.S.; McEvoy, A.J.; Mogensen, M.; Singhal, S.C.; Vohs, J. Advanced anodes for high-temperature fuel cells. *Nat. Mater.* **2004**, *3*, 17–27.
22. Brandon, N.P.; Skinner, S.; Steel, B.C.H. Recent advances in materials for fuel cells. *Annu. Rev. Mater. Res.* **2003**, *33*, 361–382.
23. Zhu, W.Z.; Deevi, S.C. A review on the status of anode materials for solid oxide fuel cells. *Mater. Sci. Eng.* **2003**, *362*, 228–239.
24. Kong, J.; Sun, K.; Zhou, D.; Zhang, N.; Mu, J.; Qiao, J. Ni-YSZ gradient anodes for anode-supported SOFCs. *J. Power Sources* **2007**, *166*, 337–342.
25. Greene, E.S.; Chiu, W.K.S.; Medeiros, M.G. Mass transfer in graded microstructure solid oxide fuel cell electrodes. *J. Power Sources* **2006**, *161*, 225–231.
26. Ni, M.; Leung, M.K.H.; Leung, D.Y.C. Micro-scale modeling of a functionally graded Ni-YSZ anode. *Chem. Eng. Technol.* **2007**, *30*, 587–592.
27. Ni, M.; Leung, M.K.H.; Leung, D.Y.C. Micro-scale modeling of solid oxide fuel cells with micro-structurally graded electrodes. *J. Power Sources* **2007**, *168*, 369–378.
28. Lee, S.J.; Jung, C.H.; Shim, K.B.; Yi, S.C. Microstructural analysis of the functionally graded electrodes in solid oxide fuel cells. *J. Ceram. Process. Res.* **2012**, *13*, 810–815.
29. Shi, J.; Xue, X. Microstructure optimization designs for anode-supported planar solid oxide fuel cells. *J. Fuel Cell Sci. Technol.* **2011**, *8*, 1011–1018.
30. Deseur, J.; Dessemond, L.; Bultel, Y.; Siebert, E. Modelling of a SOFC graded cathode. *J. Eur. Ceram. Soc.* **2005**, *25*, 2673–2676.
31. Deseur, J.; Bultel, Y.; Dessemond, L.; Siebert, E. Theoretical optimization of a SOFC composite cathode. *Electrochim. Acta* **2005**, *505*, 2037–2046.
32. Cannarozzo, M.; del Borghi, A.; Costamagna, P. Simulation of mass transport in SOFC composite electrodes. *J. Appl. Electrochem.* **2008**, *38*, 1011–1018.
33. Costamagna, P.; Costa, P.; Antonucci, V. Micro-modelling of solid oxide fuel cell electrodes. *Electrochim. Acta* **1998**, *43*, 375–394.
34. Costamagna, P.; Costa, P.; Arato, E. Some more considerations on the optimization of solid oxide fuel cell electrodes. *Electrochim. Acta* **1998**, *43*, 967–972.
35. Hussain, M.M.; Li, X.; Dincer, I. A numerical investigation of modeling an SOFC electrode as two finite layers. *Int. J. Hydrog. Energy* **2009**, *34*, 3134–3144.
36. Zheng, K.; Li, L.; Ni, M. Investigation of the electrochemical active thickness of solid oxide fuel cell anode. *Int. J. Hydrog. Energy* **2014**, *39*, 12904–12912.
37. Costamagna, P.; Honegger, K. Modeling of solid oxide heat exchanger integrated stacks and simulation at high fuel utilization. *J. Electrochem. Soc.* **1991**, *138*, 349–355.
38. Stauffer, D. *Introduction to Percolation Theory*; Taylor & Francis: London, UK, 1985.

39. Sahimi, M. *Applications of Percolation Theory*; Taylor & Francis: London, UK, 1994.
40. Bossel, U.G. *Facts and Figures*; Final Report on SOFC Data, IEA Report; Swiss Federal Office of Energy: Berne, Switzerland, 1992.
41. Costamagna, P.; Selimovic, A.; Del Borghi, M.; Agnew, G. Electrochemical model of the integrated planar solid oxide fuel cell (IP-SOFC). *Chem. Eng. J.* **2004**, *102*, 61–69.
42. Chan, S.H.; Khor, K.A.; Xia, Z.T. A complete polarization model of a solid oxide fuel cell and its sensitivity to the change of cell component thickness. *J. Power Sources* **2001**, *93*, 130–140.
43. Noren, D.A.; Hoffman, M.A. Clarifying the Butler-Volmer equation and related approximations for calculating activation losses in solid oxide fuel cell models. *J. Power Sources* **2005**, *152*, 175–181.
44. Wilson, J.R.; Kobsiriphat, W.; Mendoza, R.; Chen, H.Y.; Hiller, J.M.; Miller, D.J.; Thornton, K.; Voorhees, P.W.; Adler, S.B.; Barnett, S.A. Three-dimensional reconstruction of a solid-oxide fuel-cell anode. *Nat. Mater.* **2006**, *5*, 541–544.
45. Shearing, P.R.; Brett, D.J.L.; Brandon, N.P. Towards intelligent engineering of SOFC electrodes: A review of advanced microstructural characterization techniques. *Int. Mater. Rev.* **2010**, *55*, 347–363.
46. Kishimoto, M.; Iwai, H.; Saito, M.; Yoshida, H. Quantitative evaluation of transport properties of SOFC porous anode by random walk process. *ECS Trans.* **2009**, *25*, 1887–1896.
47. Wesselingh, J.A.; Krishna, R. *Mass Transfer in Multicomponent Mixtures*; Delft University Press: Delft, The Netherlands, 2000.
48. Mason, E.A.; Malinauskas, A.P. *Gas Transport in Porous Media: The Dusty-Gas Model*; Elsevier: Oxford, UK, 1983.
49. Bird, R.B.; Stewart, W.E.; Lighthfoot, E.N. *Transport Phenomena*; John Willey & Sons: New York, NY, USA, 1960.
50. Wilson, R.W.; Barnett, S.A. Solid oxide fuel cell Ni-YSZ anodes: Effect of composition on microstructure and performance. *Electrochem. Solid-State Lett.* **2008**, *11*, B181–B185.
51. Enrico, A.; Costamagna, P. Model of an infiltrated $\text{La}_{1-x}\text{Sr}_x\text{Co}_{1-y}\text{Fe}_y\text{O}_{3-\delta}$ cathode for intermediate temperature solid oxide fuel cells. *J. Power Sources* **2014**, doi:10.1016/j.jpowsour.2014.08.022.
52. Park, Y.M.; Lee, H.J.; Bae, H.Y.; Ahn, J.S.; Kim, H. Effect of the anode thickness on impedance response of anode-supported solid oxide fuel cells. *Int. J. Hydrog. Energy* **2012**, *11*, 4394–4400.
53. Yoon, K.J.; Gopalan, S.; Pal, U.B. Effect of the anode active layer on the performance of single-step cofired solid oxide fuel cells. *J. Electrochem. Soc.* **2008**, *155*, B610–B617.
54. Chen, K.; Chen, X.; Lü, Z.; Ai, N.; Huang, X.; Su, W. Performance of an anode-supported SOFC with anode functional layers. *Electrochim. Acta* **2008**, *53*, 7825–7830.
55. Costamagna, P.; Panizza, M.; Cerisola, G.; Barbucci, A. Effect of composition on the performance of cermet electrodes. Experimental and theoretical approach. *Electrochim. Acta* **2002**, *47*, 1079–1089.
56. Moon, H.; Kim, S.D.; Park, E.W.; Hyun, S.H.; Kim, H.S. Characteristics of SOFC single cells with anode active layer via tape casting and co-firing. *Int. J. Hydrog. Energy* **2008**, *33*, 2826–2833.
57. Kenjo, T.; Osawa, S.; Fujikawa, K. High temperature air cathodes containing ion conductive oxides. *J. Electrochem. Soc.* **1991**, *138*, 349–355.
58. Waldbilling, D.; Wood, A.; Ivey, D.G. Enhancing redox tolerance of anode-supported SOFC by microstructural modification. *J. Electrochem. Soc.* **2007**, *154*, B133–B138.

59. Zarabian, M.; Yazdan Yar, A.; Vafaenezhad, S.; Faghihi Sani, M.A.; Simchi, A. Electrophoretic deposition of functionally graded NiO-YSZ composite films. *J. Eur. Ceram. Soc.* **2013**, *33*, 1815–1823.
60. Menzler, N.H.; Malzbender, J.; Schöderbock, P.; Kauert, R.; Buchkremer, H.P. Sequential tape casting of anode-supported solid oxide fuel cells. *Fuel Cells.* **2014**, *14*, 96–106.
61. Orui, H.; Nozawa, K.; Watanabe, K.; Sugita, S.; Chiba, R.; Komatsu, T.; Arai, H.; Arakawa, M. Development of practical size anode-supported solid oxide fuel cells with multilayer anode structures. *J. Electrochem. Soc.* **2008**, *155*, B1110–B1116.
62. Haanappel, V.A.C.; Mertens, J.; Rutenbeck, D.; Tropartz, C.; Sebold, D.; Tietz, F. Optimization of processing and microstructural parameters of LSM cathodes to improve the electrochemical performance of anode-supported SOFCs. *J. Power Sources* **2005**, *141*, 216–226.

© 2014 by the authors; licensee MDPI, Basel, Switzerland. This article is an open access article distributed under the terms and conditions of the Creative Commons Attribution license (<http://creativecommons.org/licenses/by/3.0/>).